

# On the large-scale outflows in active galactic nuclei: consequences of coupling the mass-supply rate and accretion luminosity

Ryuichi Kurosawa<sup>\*</sup>, and Daniel Proga

*Department of Physics and Astronomy, University of Nevada Las Vegas, Box 454002, 4505 Maryland Pkwy, Las Vegas, NV 89154-4002, USA*

Dates to be inserted

## ABSTRACT

We present two-dimensional hydrodynamical simulations of slowly rotating gas that is under the influence of the gravity of a super massive black hole and is irradiated by a thin UV accretion disc and a spherical X-ray corona. We calculate the accretion luminosity of a system based on the accretion-rate which is assumed to be equal to the mass-supply rate at the radius of  $\sim 10^{-2}$  pc. For the models with high temperature gas at large radii ( $\sim 10$  pc) and high luminosities, we find a strong correlation between the mass-outflow rate ( $\dot{M}_{\text{out}}$ ) and the luminosity ( $L$ ). The power law index ( $q$ ) describing the  $\dot{M}_{\text{out}}-L$  relation is  $q = 2.0 (\pm 0.1)$ , which is very similar to that for radiation-driven stellar and disc wind models. More surprisingly, for high density at large radii, we find steady state solutions with the accretion luminosity *exceeding* the Eddington limit. The super-Eddington accretion proceeds in the equatorial region and is possible because the radiation flux from the disc is significantly reduced in the equatorial direction due to the geometrical foreshortening effect. In all models, an outflow is driven from an inflow with sub-Keplerian rotation. For high temperature at large radii, the inflow occurs over a wide range of the polar angles, and the outflow occurs in a relatively narrow polar cone. However, for the super-Eddington cases with low temperature at large radii, the inflow persists only very close to the equatorial plane, resembling a thin accretion disc, while the outflow arises in a wide range of radii and polar angles. The geometry of this extreme inflow-outflow solution is very similar to a radiation-driven wind from a luminous Keplerian accretion disc. For the cold super-Eddington solutions,  $\dot{M}_{\text{out}}$  is only very weakly correlated with  $L$ , i.e.  $0 \lesssim q \lesssim 0.2$ . This weaker correlation is mainly caused by a mismatch between the direction of escaping photons and the inflowing gas: the radiation is emitted mostly in the polar directions whereas the inflowing gas occurs mainly in the equatorial region.

## Key words:

accretion, accretion discs – hydrodynamics – galaxies: kinematics and dynamics – methods: numerical – galaxies: active

## 1 INTRODUCTION

Induced by accretion of gas on to a super massive ( $10^6-10^{10} M_{\odot}$ ) black hole (SMBH), active galactic nuclei (AGN) release a large amount of energy by radiating photons ( $10^{10}-10^{14} L_{\odot}$ ). These photons influence the physical properties (e.g. the ionization structure, gas dynamics and density distribution) of the vicinity of AGN, the AGN host galaxies, and the inter-galactic media of galaxy clusters to which they belong (e.g. Quilis, Bower, & Balogh 2001; Dalla Vecchia et al. 2004; McNamara et al. 2005; Zanni et al. 2005; Fabian et al. 2006; Vernaleo & Reynolds 2006). Importance of the feedback from AGN has been recognised in many areas of astrophysics, e.g. (i) co-evolution of galaxies and black holes (e.g. Ciotti & Ostriker 1997, 2001, 2007; King

2003; Hopkins et al. 2005; Murray, Quataert, & Thompson 2005; Sazonov et al. 2005; Di Matteo, Springel, & Hernquist 2005; Springel, Di Matteo, & Hernquist 2005a; Brighenti & Mathews 2006; Fontanot et al. 2006; Wang, Chen, & Hu 2006; Tremonti, Moustakas, & Diamond-Stanic 2007; Yuan et al. (2009); Ciotti, Ostriker, & Proga 2009), (ii) star formation in host galaxies (e.g. Hamann & Ferland 1992; Maloney 1999; Murray, Quataert, & Thompson 2005; Kim, Ho, & Im 2006; Schawinski et al. 2009a; Schawinski et al. 2009b), (iii) the so-called cooling flow problem in galaxy clusters (e.g. Binney & Tabor 1995; Tucker & David 1997; Soker & Pizzolato 2005; Scannapieco, Silk, & Bouwens 2005; Rafferty, McNamara, Nulsen, & Wise 2006; McNamara & Nulsen 2007; Guo, Oh, & Ruszkowski 2008; Rafferty, McNamara, & Nulsen 2008).

The form of AGN feedback can be mechanical

<sup>\*</sup> E-mail:rk@physics.unlv.edu

(e.g. Binney & Tabor 1995; Begelman & Nath 2005; Springel, Di Matteo, & Hernquist 2005b) or radiative in which photon momentum, energy or both are dynamically important (e.g. Ciotti & Ostriker 1997, 2001, 2007; Ciotti et al. 2009). The radiation can produce mechanical feedback via radiation pressure on matter in the form of outflows/winds (e.g. Proga 2007; Proga, Ostriker, & Kurosawa 2008; Dorodnitsyn, Kallman, & Proga 2008a,b; Kurosawa & Proga 2008, 2009). A strong support for the existence of such (radiation-driven) winds is often found in the highly blueshifted broad absorption line features seen in the UV and optical spectra of AGN (e.g. Murray et al. 1995; Proga, Stone, & Kallman 2000; Chartas, Brandt, & Gallagher 2003; Crenshaw, Kraemer, & George 2003; Proga & Kallman 2004; Hamann et al. 2008), provided the ionization state of the gas is appropriate. We note that the outflows can be also produced by magnetocentrifugal force (e.g. Blandford & Payne 1982; Emmering, Blandford, & Shlosman 1992; Königl & Kartje 1994; Bottorff et al. 1997), Poynting flux/magnetic towers (e.g. Lovelace, Wang, & Sulkanen 1987; Lynden-Bell 1996, 2003; Li et al. 2001; Proga 2003; Kato, Mineshige, & Shibata 2004; Nakamura, Li, & Li 2006; Kato 2007), and thermal pressure (e.g. Weymann et al. 1982; Begelman, de Kool, & Sikora 1991; Everett & Murray 2007).

In our previous studies (Proga 2007; Proga et al. 2008; Kurosawa & Proga 2009, hereafter Papers I, II and III, respectively), we performed hydrodynamical simulations of radiatively driven AGN outflows produced from the infalling gas. Our models include radiation forces due to electron scattering and line processes, and radiative cooling/heating. These models use a fixed accretion luminosity during the whole simulations regardless of the mass inflow rate through the model inner boundary. In principle, the rate at which the gas is supplied to the region below the inner boundary ( $\sim 10^{-2}$  pc) would influence the mass accretion rate on to the SMBH at the centre and its luminosity. This could result in models with an inconsistent amount of the radiative feedback for a given amount of the mass supplied rate to the inner region of AGN. Here we relax this assumption of the constant luminosity, and instead dynamically couple the accretion luminosity to the mass supply rate. With this coupling, we examine the following two key issues in this study.

Firstly, we investigate how the mass-outflow rate depends on the self-consistently determined accretion luminosity (or equivalently the Eddington ratio  $\Gamma$  of the system). This provides a useful information on the mass supply rate and the mass inflow morphology which can be incorporated with a smaller scale disc accretion model (e.g. Ohsuga 2007). Similarly, the mass-outflow rates predicted here can be incorporated with a larger scale galaxy evolution model (e.g. Ciotti et al. 2009).

Secondly, we test whether steady state solutions with a super-Eddington luminosity are possible when the main radiation source has a disc geometry instead of a spherical geometry. The system with the disc radiation field has a possible channel of a high mass supply rate along an equatorial plane at a large distance from the disc itself. Because of the disc geometry, the radiation would peak strongly along the pole or disc axis directions, and it would gradually decrease toward equatorial direction hence the radiation force is much weaker in the equatorial plane.

In the following section, we describe our method and model assumptions. We give the results of our hydrodynamical simulations in Section 3. Discussions on accretion flows with a super-Eddington luminosity and the effect of artificially limiting lumi-

nosity are given in Section 4. Finally, the conclusions of this study are summarised in Section 5.

## 2 METHOD

### 2.1 Overview

We mainly follow the methods used for the axisymmetric models by Proga et al. (2000) and Proga & Kallman (2004), but with a change in the treatment of the accretion luminosity (Section 2.4). The model geometry and the assumptions of the SMBH and the disc are very similar to those in Papers I, II and III. Readers are referred to Fig. 1 of Paper III for the diagram of our basic model configuration. A SMBH with its mass  $M_{\text{BH}}$  and its Schwarzschild radius  $R_{\text{S}} = 2GM_{\text{BH}}/c^2$  is placed at the centre of the polar coordinate system  $(r, \theta)$ . The X-ray emitting corona region is defined as a sphere with its radius  $r_*$  which surrounds the SMBH. The geometrically thin and optically thick accretion disc (e.g. Shakura & Sunyaev 1973) is placed on the equatorial plane ( $\theta = \pi/2$  plane). The normal vector of the disc coincides with the symmetry axis. The hydrodynamic simulations will be performed in the polar coordinate system (assuming axisymmetry) with  $r$  between the inner boundary  $r_{\text{i}}$  and the outer boundary  $r_{\text{o}}$ . The radiation forces, from the corona region (the sphere with its radius  $r_*$ ) and the accretion disc, acting on the gas are assumed to be radial only. The point-source like approximation for the disc radiation pressure is used here since the accretion disc radius ( $r_{\text{D}}$ ) is assumed to be much smaller than the inner radius, i.e.  $r_{\text{D}} \ll r_{\text{i}}$ .

Because of the assumed flat accretion disc geometry, the disc radiation flux ( $\mathcal{F}_{\text{disc}}$ ) peaks in the direction of the disc rotational axis, and it gradually decreases as the polar angle  $\theta$  increases, i.e.  $\mathcal{F}_{\text{disc}} \propto |\cos \theta|$ . The flow is also irradiated by the corona which is assumed to be spherical. Further, we assume that the total accretion luminosity  $L$  consists of two components: (1)  $L_{\text{disc}} = f_{\text{disc}}L$  due to the accretion disc and (2)  $L_* = f_*L$  due to the corona (i.e.  $f_{\text{disc}} + f_* = 1$ ). We assume that the disc emits only UV photons, whereas the corona emits only X-rays, i.e. the system UV luminosity,  $L_{\text{UV}} = f_{\text{UV}}L = L_{\text{disc}}$  and the system X-ray luminosity,  $L_{\text{X}} = f_{\text{X}}L = L_*$  (in other words  $f_{\text{UV}} = f_{\text{disc}}$  and  $f_{\text{X}} = f_*$ ).

We include the effect of radiation forces due to electron scattering and line processes (line force). To evaluate the line force, we follow the method described by Proga et al. (2000) who use a modified version of the formalism developed by Castor, Abbott, & Klein (1975) (CAK model). In our model, the line force is evaluated by using the analytical formulae of Stevens & Kallman (1990) who parametrised the force in terms of the photoionization parameter, defined as  $\xi = 4\pi\mathcal{F}_{\text{X}}/n$  where  $\mathcal{F}_{\text{X}}$  and  $n$  are the local X-ray flux and the number density of the gas, respectively. This parametrisation of the line force is computationally efficient and it provides good estimates for the number and opacity distribution of spectral lines for a given  $\xi$ .

Note that we account for the attenuation of X-ray radiation by computing X-ray optical depth in radial direction; however, we assume that the gas is optically thin in UV. The assumption of no attenuation of UV radiation has to be made in our formalism since the photoionization model of Stevens & Kallman (1990) does not include the UV attenuation; therefore, to be consistent with their model. We will discuss the validity of this assumption later in Section 4.4.

With the simplification above, only the corona (X-ray) radiation contributes to bringing atoms to very high ionization states.

We assume that the corona contributes to the radiation force due to electron scattering, but not to the line force although some metal lines in the soft X-ray may contribute to the line force in some cases. On the other hand, the disc radiation (UV) contributes significantly to the line force and the force due to electron scattering.

In all the models presented in this work, we assume that the inflowing gas at the outer boundary is very slowly rotating, i.e. the rotation velocity of the gas is much smaller than the Keplerian velocity. We use the same specific angular momentum distribution of the gas at the outer boundary as in Paper III.

## 2.2 Hydrodynamics

We employ hydrodynamical (HD) simulations of the outflow from accretion on to a central part of AGN in 2-D (axisymmetric), using the ZEUS-MP code (cf. Hayes et al. 2006) which is a massively parallel MPI-implemented version of the ZEUS-3D code (cf., Hardee & Clarke 1992; Clarke 1996). The ZEUS-MP is a Eulerian hydrodynamics code which uses the method of finite differencing on a staggered mesh with a second-order-accurate, monotonic advection scheme (Hayes et al. 2006). To compute the structure and evolution of a flow irradiated by a strong continuum radiation of AGN, we solve the following set of HD equations:

$$\frac{D\rho}{Dt} + \rho \nabla \cdot \mathbf{v} = 0, \quad (1)$$

$$\rho \frac{D\mathbf{v}}{Dt} = -\nabla P + \rho \mathbf{g} + \rho \mathbf{g}_{\text{rad}}, \quad (2)$$

$$\rho \frac{D}{Dt} \left( \frac{e}{\rho} \right) = -P \nabla \cdot \mathbf{v} + \rho C, \quad (3)$$

where  $\rho$ ,  $e$ ,  $P$  and  $\mathbf{v}$  are the mass density, energy density, pressure, and the velocity of gas respectively. Also,  $\mathbf{g}$  is the gravitational force per unit mass. The Lagrangian/co-moving derivative is defined as  $D/Dt \equiv \partial/\partial t + \mathbf{v} \cdot \nabla$ . We have introduced two new components to the ZEUS-MP in order to treat the gas dynamics more appropriate for the flow in and around AGN. The first is the acceleration due to radiative force per unit mass ( $\mathbf{g}_{\text{rad}}$ ) in equation 2, and the second is the effect of radiative cooling and heating, simply as the net cooling rate ( $C$ ) in equation 3. We assume the equation of state to be in the form of  $P = (\gamma - 1)e$  where  $\gamma$  is the adiabatic index, and  $\gamma = 5/3$  for all the models presented in this paper. Our numerical method used in this paper are identical, in most aspects, to that described in Papers I and II. Next, we briefly discuss our implementation of  $\mathbf{g}_{\text{rad}}$  and  $C$ .

## 2.3 Radiation force and radiative heating/cooling

As mentioned earlier, we consider two different continuum radiation sources in our models: (1) the accretion disc, and (2) the central spherical corona. In the point-source approximation limit, the radiation flux from the central X-ray corona region can be written as

$$\mathcal{F}_* = \frac{L_*}{4\pi r^2} \quad (4)$$

where  $r$  is the radial distance from the centre (by neglecting the source size). Here we neglect the geometrical obscuration of the corona emission by the accretion disc and vice versa. On the other hand, the disc radiation depends on the polar angle  $\theta$  because of the source geometry. Again following Papers I and II (see also Proga et al. 1998), the disc flux  $\mathcal{F}_{\text{disc}}$  is assumed to be radial and

$\mathcal{F}_{\text{disc}} \propto |\cos \theta|$ . Consequently, the disc radiation flux at a distance  $r$  from the centre can be written as

$$\mathcal{F}_{\text{disc}} = 2 |\cos \theta| \frac{L_{\text{disc}}}{4\pi r^2} \quad (5)$$

where  $\theta$  is the polar angle (angle between the disc normal and the position vector  $\mathbf{r}$ ). The leading term 2 in this expression comes from the normalisation of the flux.

To evaluate the radiative acceleration due to line force, we follow the method in Proga et al. (2000) (see also Proga et al. 1998) who applied the modified version of CAK model (see also Castor et al. 1975). Their model works under the assumption of the Sobolev approximation (e.g., Sobolev 1957; Castor 1970; Lucy 1971). Following Proga et al. (2000), the radiative acceleration of a unit mass at a point  $\mathbf{r}$  can be written as

$$\mathbf{g}_{\text{rad}} = \oint_{\Omega} [1 + \mathcal{M}] \left[ \frac{\sigma_e I(\mathbf{r}, \hat{\mathbf{n}})}{c} \right] \hat{\mathbf{n}} d\Omega \quad (6)$$

where  $I$ ,  $\Omega$  and  $\sigma_e$  are the frequency-integrated continuum intensity in the direction  $\hat{\mathbf{n}}$ , the solid angle subtended by the source of continuum radiation, and the electron scattering cross section, respectively. The force multiplier  $\mathcal{M}$  is a function of optical depth parameter  $\tau'$  which is similar to the Sobolev optical depth (c.f. Rybicki & Hummer 1978). The parameters in  $\mathcal{M}$  are functions of the photoionization parameter  $\xi$  (Stevens & Kallman 1990). Using eqs. (4), (5), (6), and the luminosity ratios ( $f_*$  and  $f_{\text{disc}}$ ), the radiative acceleration term in equation 2 can be reduced to

$$\mathbf{g}_{\text{rad}} = \frac{\sigma_e L}{4\pi r^2 c} [f_* + 2f_{\text{disc}}(1 + \mathcal{M})|\cos \theta|] \hat{\mathbf{r}}. \quad (7)$$

To evaluate the gas temperature, we follow the method described by Proga et al. (2000) and Proga & Kallman (2004). The model includes some effects of photoionization. The gas is assumed to be optically thin to its own cooling radiation. The radiative processes included are Compton heating/cooling, X-ray photoionization and recombination, bremsstrahlung, and line cooling. The net cooling rate depends on the photoionization parameter  $\xi$  and the characteristic temperature of the X-ray radiation ( $T_X$ ). For more detail, readers are referred to Papers I and II (see also Proga et al. 2000) for our implementations of  $\mathbf{g}_{\text{rad}}$  and  $C$ .

Note that the angular distribution of the radiation in equation 7 and also the luminosity ratios ( $f_*$  and  $f_{\text{disc}}$ ) are fixed during the whole simulations. In other words, the radiation from the disc (equation 5) and the X-ray corona region (equation 4) are treated as inner boundary conditions; hence, they are not self-consistently determined while the simulations proceed.

## 2.4 Coupling of Mass-Accretion Rate and Luminosity

In our previous models (Papers I, II and III), the accretion luminosity of the system is kept fixed. Consequently, the radiative feedback may not be consistent with the mass supplied to the inner region of AGN transferred from our inner boundary. To overcome this possible inconsistency of the accretion luminosity and the mass inflow rate, we relax the assumption of the constant luminosity. The luminosity is now coupled to the mass-accretion rate ( $\dot{M}_a$ ) in the following way. At each time step, the accretion luminosity is adjusted based on the history of the mass accretion rate through the inner boundary. However, since our inner boundary is rather large compare to  $r_*$ , we introduce a lag time ( $\tau$ ). The lag time roughly corresponds to the accretion time scale for the gas to reach the BH from the inner boundary of our computational domain. This should naturally cause a self-regulation of mass-accretion rate and

the amount of radiative feedback, i.e. a higher mass accretion rate hence a higher accretion luminosity will more strongly push surrounding gas outward, and will naturally slow down the accretion process.

The mass accretion rate of the BH with mass  $M_{\text{BH}}$  at a given time  $t$  is  $\dot{M}_{\text{a}}(t)$ , the accretion luminosity is given by

$$L(t) = \frac{2\eta G M_{\text{BH}} \dot{M}_{\text{a}}(t)}{R_{\text{S}}} \quad (8)$$

where  $\eta$ ,  $G$  and  $R_{\text{S}}$  are the rest mass conversion efficiency, the gravitational constant, and the Schwarzschild radius of the BH, respectively. The growth rate of black hole mass is negligible here in the time scale used in our simulation. We estimate the mass accretion rate at a given time  $t$  by computing the time average of the mass inflow rate ( $\dot{M}$ ) at the inner boundary as our simulation proceeds. If the time duration used for the averaging the mass accretion rate is  $\Delta t$ , then we can write the average mass accretion rate ( $\dot{M}_{\text{a}}$ ) as

$$\dot{M}_{\text{a}}(t) = \frac{\int_{t-\tau-\Delta t}^{t-\tau} \dot{M}(t') dt'}{\int_{t-\tau-\Delta t}^{t-\tau} dt'} \quad (9)$$

In our models we set  $\Delta t = \tau$ , and the denominator simply becomes  $\tau$ . In the ‘standard’  $\alpha$  disc models, the accretion timescale ( $t_{\text{acc}}$ ) or the lag time  $\tau$  can be approximated as  $t_{\text{acc}} = \mathcal{O}(t_{\text{dyn}}/\alpha)$  where  $t_{\text{dyn}}$  and  $\alpha$  are the dynamical timescale at the outer radius ( $r_{\text{d}}$ ) of the disc and the  $\alpha$  viscosity parameter (Shakura & Sunyaev 1973). In this paper, we assume  $r_{\text{d}} = 2.6 \times 10^{16}$  cm and  $\alpha = 0.1$ , which give  $t_{\text{dyn}} \approx 10^8$  s, and consequently  $\tau = t_{\text{acc}} \approx 10^9$  s (see also Ciotti & Ostriker 2001 for a similar treatment). Note that the time scale for the free-falling gas ( $t_{\text{ff}}$ ) to reach the centre from the inner boundary of our computational domain is approximately  $10^8$  s which is same order of magnitude as the dynamical timescale mentioned above. For the models which has a steady state solutions, we find that the basic flow properties (e.g. morphology, mass-accretion rate, and gas temperature) are rather insensitive to the value of  $\tau$ .

A caveat in the method described here is that we assume all the inflowing gas which crosses the inner boundary reaches the accretion disc and contributes to the accretion luminosity. In reality, some fraction of the gas which falls inward of the inner boundary may not reach the accretion disc due to, again, strong disc radiation (e.g. Proga et al. 2000).

## 2.5 Model Setup

The following parameters are common to all the models presented here, and are exactly same as in Papers I, II and III. We assume that the central BH is non-rotating and has mass  $M_{\text{BH}} = 10^8 M_{\odot}$ . The size of the disc inner radius is assumed to be  $r_* = 3 R_{\text{S}} = 8.8 \times 10^{13}$  cm. The rest mass conversion efficiency ( $\eta$ ) in equation 8 is assumed to be 0.0833. The Eddington luminosity of the Schwarzschild BH, i.e.  $4\pi c G M_{\text{BH}} / \sigma_e$  for our system is about  $1.3 \times 10^{46}$  erg s $^{-1}$  or  $3.3 \times 10^8 L_{\odot}$ . The fractions of the luminosity in the UV ( $f_{\text{UV}}$ ) and that in the X-ray ( $f_{\text{X}}$ ) are fixed at 0.95 and 0.05 respectively, as in Paper I (their Run C) and in Paper II (their Run Cr). These two parameters determine the shape of the underlying continuum emission of the central source (cf. Section 2.2).

The following ranges of the coordinates are adopted:  $r_{\text{i}} \leq r \leq r_{\text{o}}$ ,  $0 \leq \theta \leq \pi/2$  where  $r_{\text{i}} = 500 r_*$  and  $r_{\text{o}} = 2.5 \times 10^5 r_*$ . The radius of the central and spherical X-ray corona region  $r_*$  coincides the inner radius of the the accretion disc. In our simulations, the polar angle range is divided into 64 zones, and are equally spaced.

In the  $r$  direction, the gird is divided into 140 zones in which the zone size ratio is fixed at  $\Delta r_{k+1} / \Delta r_k = 1.04$ .

For the initial conditions, the density and the temperature of gas are set uniformly, i.e.  $\rho = \rho_{\text{o}}$  and  $T = T_{\text{o}}$  everywhere in the computational domain (Table 1). The initial velocity of the gas is assigned by assuming the same specific angular momentum distribution used in Papers II and III. At the inner and outer boundaries ( $r_{\text{i}}$  and  $r_{\text{o}}$ ), we apply the outflow (free-to-outflow) boundary conditions, in which the field values are extrapolated beyond the boundaries using the values of *the ghost zones* residing outside of normal computational zones (see Stone & Norman 1992 for more details). At  $r = r_{\text{o}}$ , all HD quantities are assigned to the initial conditions (e.g.  $T = T_{\text{o}}$  and  $\rho = \rho_{\text{o}}$ ) during the evolution of each model; however, this outer boundary condition is applied only when the gas is inflowing at  $r = r_{\text{o}}$ , i.e. when  $v_r < 0$ . The radial component of the velocity is allowed to float (unconstrained) when  $v_r > 0$  at  $r = r_{\text{o}}$ . In Paper II, we also applied these conditions to represent a steady flow condition at  $r = r_{\text{o}}$ . We found that this technique leads to a solution that relaxes to a steady state in both spherical and non-spherical accretion with an outflow (see also Proga & Begelman 2003). This imitates the condition in which a continuous supply of gas is available at  $r = r_{\text{o}}$ . We also consider a several cases in which the temperature at  $r = r_{\text{o}}$  is unconstrained (Section 4.3).

## 2.6 Reference Values

Important reference physical quantities relevant to our systems are as follows. The Compton radius,  $R_{\text{C}} \equiv GM_{\text{BH}} \mu m_p / k T_{\text{C}}$ , is  $8 \times 10^{18}$  cm or equivalently  $9 \times 10^4 r_*$  where  $T_{\text{C}}$ ,  $\mu$  and  $m_p$  are the Compton temperature, the mean molecular weight of gas and the proton mass, respectively. We assume  $T_{\text{C}} = 2 \times 10^7$  K and  $\mu = 1$ . The corresponding speed of sound at infinity is  $c_{\infty} = (\gamma k T_{\text{C}} / \mu m_p)^{1/2} = 4 \times 10^7$  cm s $^{-1}$ . The corresponding Bondi radius (Bondi 1952) is  $R_{\text{B}} = GM_{\text{BH}} / c_{\infty}^2 = 4.8 \times 10^{18}$  cm while its relation to the Compton radius is  $R_{\text{B}} = \gamma^{-1} R_{\text{C}}$ . The Bondi accretion rate (for the isothermal flow) is  $\dot{M}_{\text{B}} = 3.3 \times 10^{25}$  g s $^{-1} = 0.52 M_{\odot}$  yr $^{-1}$ . The corresponding free-fall time ( $t_{\text{ff}}$ ) of gas from the Bondi radius to the inner boundary is  $2.1 \times 10^{11}$  sec =  $7.0 \times 10^3$  yr. The escape velocity from the inner most radius ( $r_{\text{i}} = 500 r_*$ ) of the computational domain is about  $7.7 \times 10^4$  km s $^{-1}$ .

## 3 RESULTS

We examine the effect of changing the outer boundary conditions on the gas property, flow morphology and gas dynamics. Here, we focus on two key parameters, i.e. density ( $\rho_{\text{o}}$ ) and temperature ( $T_{\text{o}}$ ) at  $r = r_{\text{o}}$ . We consider three different temperatures:  $T_{\text{o}} = 2 \times 10^6$ ,  $2 \times 10^7$  and  $2 \times 10^8$  K with a wide range of  $\rho_{\text{o}}$ . In total, 22 combinations of  $\rho_{\text{o}}$  and  $T_{\text{o}}$  are considered. The model parameters along basic results are summarised in Table. 1.

### 3.1 Dependency of Mass Outflow Rates on Accretion Luminosity

First, we examine how mass outflow rates of systems depend on the accretion luminosity that is self-consistently determined. Fig. 1 shows the mass outflow rate at the outer boundary  $\dot{M}_{\text{out}}(r_{\text{o}})$  plotted as a function of the accretion luminosity, or equivalently as a function of the Eddington ratio  $\Gamma$  ( $\equiv L/L_{\text{Edd}}$  where  $L_{\text{Edd}} =$

**Table 1.** Summary of models with different combinations of  $\rho_o$  and  $T_o$ 

Model	$\rho_o$ ( $10^{-21}$ g cm $^{-3}$ )	$T_o$ ( $10^7$ K)	$\dot{M}_{in}(r_i)$ ( $10^{25}$ g s $^{-1}$ )	$\Gamma$ ...	$\dot{M}_{out}(r_o)$ ( $10^{25}$ g s $^{-1}$ )	Variability ...	Outflow Morphology ...
1	1	0.2	5.1(0.002) <sup>‡</sup>	0.30(0.001) <sup>‡</sup>	0.0(0.0) <sup>‡</sup>	steady	no outflow
2	2	0.2	8.6(0.14)	0.51(0.01)	1.4(1.3)	steady	polar
3	3	0.2	11(0.36)	0.65(0.02)	3.4(2.1)	semi-steady	wide polar
4	5	0.2	15(1.8)	0.89(0.11)	6.2(3.1)	semi-steady	wide polar
5	10	0.2	22(2.3)	1.3(0.1)	13(4.6)	semi-steady	wide polar
6	20	0.2	36(3.8)	2.1(0.2)	17(7.7)	semi-steady	disc wind
7	50	0.2	63(8.6)	3.8(0.5)	21(16)	semi-steady	disc wind
8	100	0.2	93(6.2)	5.5(0.4)	18(13)	semi-steady	disc wind
9	200	0.2	130(5.0)	7.7(0.3)	20(12)	semi-steady	disc wind
...	...	...	...	...	...	...	...
10	0.4	2	2.4(0.01)	0.14(0.01)	0.0(0.0)	steady	no outflow
11	1	2	8.3(0.36)	0.49(0.02)	2.0(2.3)	semi-steady	narrow conic
12	2	2	15(6.5)	0.89(0.38)	9.4(11)	semi-steady	conic
13	4	2	26(13)	1.5(0.8)	24(22)	semi-steady	wide conic
14	10	2	56(31)	3.3(1.8)	66(91)	semi-steady	wide conic
...	...	...	...	...	...	...	...
15	0.5	20	1.3(4.9)	0.074(0.292)	3.4(4.5)	spiky	almost spherical
16	1	20	2.8(5.6)	0.17(0.33)	4.3(4.2)	spiky	spherical/polar
17	1.5	20	7.5(13)	0.45(0.77)	7.1(9.1)	spiky	polar
18	2	20	19(0.072)	1.1(0.043)	13(0.51)	steady	polar
19	3	20	29(0.080)	1.7(0.047)	31(2.6)	steady	polar
20	4	20	39(0.31)	2.3(0.02)	54(16)	steady	conic
21	6	20	58(3.0)	3.5(0.2)	113(47)	semi-steady	conic
22	8	20	77(3.6)	4.6(0.2)	169(66)	semi-steady	wide conic
...	...	...	...	...	...	...	...
23*	1	2	8.3(0.38)	0.49(0.02)	2.0(1.8)	semi-steady	narrow conic
24*	2	2	16(4.7)	0.95(0.28)	12(7.0)	semi-steady	conic
25*	4	2	40(13)	2.4**(0.77)	14(11)	semi-steady	conic
26*	10	2	140(91)	8.3**(5.4)	23(41)	semi-steady	conic
...	...	...	...	...	...	...	...
27 <sup>†</sup>	1	2	4.7(0.29)	0.27(0.02)	5.4(1.5)	semi-steady	conic

(\*) Luminosity is limited to  $\Gamma \leq 1$  and not completely self-consistent.

(\*\*)  $\Gamma$  value corresponds to the luminosity which would have been achieved in the system is if the luminosity is computed from the mass accretion rate listed in the previous column.

(†) Fixed luminosity model in Proga et al. (2008) (their Run Cr) and Kurosawa & Proga (2009) (their Model II).

(‡) Values in brackets are the standard deviations of the time series values.

**Table 2.** Summary of power-law fits for the  $\dot{M}_{out}-\Gamma$  relations

Main wind driving force	$T$ ( $10^7$ K)	$\Gamma$ range	$q^{**}$
Radiation	all*	$\sim 0.5$ to $\sim 5$	2.0( $\pm 0.1$ )
Radiation	0.2	$\sim 0.5$ to $\sim 1.4$	2.3( $\pm 0.3$ )
Radiation	2	$\sim 0.5$ to $\sim 3$	1.8( $\pm 0.2$ )
Radiation	20	$\sim 0.9$ to $\sim 5$	1.8( $\pm 0.1$ )
...	...	...	...
Thermal	20	$\lesssim 0.7$	0.4( $\pm 0.1$ )
Radiation ('disc-wind')	0.2	$\gtrsim 1.4$	0.1( $\pm 0.1$ )

(\*) Used the points from all three temperatures (excluding points for Models 6, 7, 8, 9, 15, 16 and 17)

(\*\*) The index of the power-law, i.e.  $\dot{M}_{out} \propto \Gamma^q$ . The radiation-driven stellar wind model of Castor et al. (1975) finds  $q = 1.67$ .

$4\pi cGM_{BH}/\sigma_e$ ) for different combinations of  $\rho_o$  and  $T_o$ . The actual values for  $\dot{M}_{out}(r_o)$  and  $\Gamma$  (along with the corresponding mass inflow fluxes at the inner boundary  $\dot{M}_{in}$ ) are also listed in Table 1. Note that  $\dot{M}_{out}$  values used here are the time-averaged values since the mass inflow rate  $\dot{M}_{in}$  or equivalently mass accretion rate  $\dot{M}_a$  in

some of the models (as also indicated in the table) show some degree of variability, which will be discussed later in Section 3.2.

The figure shows that most of the data points follow the lines that cross the panel almost diagonally, displaying strong correlations between  $\dot{M}_{out}$  and  $\Gamma$ . The outflows formed in the models with  $\Gamma \gtrsim 0.5$  are mainly *radiatively driven* whereas those in the highest temperature cases ( $T_o = 2 \times 10^8$  K) with  $\Gamma \lesssim 0.5$  (Models 15, 16 and 17) are mainly *thermally driven*.

The models with the lowest temperature ( $T_o = 2 \times 10^6$  K) follow the main trend defined by the data points for the models with the radiation-driving dominated outflows for  $0.5 \lesssim \Gamma \lesssim 1.5$ . No outflow forms for  $\Gamma \lesssim 0.5$ . The mass outflow rates become saturated at higher  $\Gamma$  values ( $\Gamma \gtrsim 1.5$ ), i.e. the strength of the correlation weakens dramatically. The cause of the saturation seen in the the low temperature models will be discussed later in Section 3.3. The models with  $T_o = 2 \times 10^7$  K shows a correlation between  $\dot{M}_{out}$  and  $\Gamma$  for all models with  $\Gamma \gtrsim 0.5$ . Again no outflow forms for  $\Gamma \lesssim 0.5$ . The figure also shows a point for the model run (Model 27) with the same parameters as in Model 11 ( $\rho_o = 1 \times 10^{-21}$  g cm $^{-3}$  and  $T_o = 2 \times 10^7$  K), but with a fixed accretion luminosity ( $\Gamma = 0.6$ ). Note that this model is equivalent to Run Cr in Paper II, and Model II in Paper III. These fixed  $\Gamma$  (con-

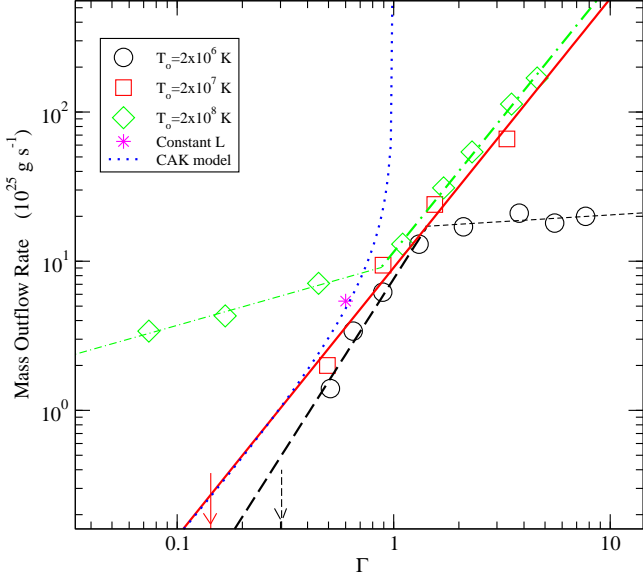


**Figure 1.** Comparisons of the relations between the mass outflow rates ( $\dot{M}_{\text{out}}$  through the outer boundary) and the Eddington ratio ( $\Gamma$ ) for the models with three different ambient gas temperatures ( $T_o$ ):  $2 \times 10^6$  (circles),  $2 \times 10^7$  (squares) and  $2 \times 10^8$  K (diamonds). The parameters used for the models/data points are summarised in Table 1. The points along the diagonal lines (thick lines) clearly shows that  $\dot{M}_{\text{out}}$  correlates with  $\Gamma$  for all  $T_o$ . The strong correlation is seen in the lowest temperature models ( $T_o = 2 \times 10^6$  K) for  $0.5 \lesssim \Gamma \lesssim 1.5$ , but  $\dot{M}_{\text{out}}$  becomes saturated at the higher  $\Gamma$  values ( $\Gamma \gtrsim 1.5$ ; cf. Sec. 3.3). For the models with  $T_o = 2 \times 10^7$  K, a correlation is seen for all the points with  $\Gamma \gtrsim 0.5$ . The high temperature models ( $T_o = 2 \times 10^8$  K) show two distinctive regions in which the points follow two different slopes. The outflows in the models for  $\Gamma \lesssim 1$  (Models 15, 16 and 17) are *mainly thermally driven*, but the models with  $\Gamma \gtrsim 1$  are *mainly radiation-driven*. The thermal winds found here are artifacts of the inner boundary. A simple power law is used to fit the points for the models with the outflows mainly driven by radiation, for each temperature:  $2 \times 10^6$  (thick dashed line),  $2 \times 10^7$  (thick solid line) and  $2 \times 10^8$  K (thick dash-dot line). A separate power law (thin dashed line) is used for the points with four largest  $\Gamma$  (Models 6, 7, 8 and 9) in the  $T_o = 2 \times 10^6$  K models, and another power law is used for the models with the thermally driven outflows with  $T_o = 2 \times 10^8$  K (Models 15, 16 and 17). The indices of the power law fits are summarised in Table 2. The mass-loss rate predicted by the radiation-driven stellar wind model (dotted line) by Castor et al. (1975) (CAK model) is also shown for a comparison. The arrows near the bottom of the panel indicate the approximate location of the Eddington ratios for the models below which an outflow does not form. The solid and dashed arrows are for the models with  $T_o = 2 \times 10^6$  and  $2 \times 10^7$  K, respectively. The constant luminosity ( $\Gamma = 0.6$ ) model (star), as in Papers II and III (with  $T_o = 2 \times 10^7$  K and  $\rho_o = 1 \times 10^{-21}$  g cm $^{-3}$ ), is also shown for a comparison (Model 27).

stant  $L$ ) models are located near the main trend of the  $\dot{M}_{\text{out}} - \Gamma$  relation found here. This reassures that our previous models parameters ( $\Gamma$ ,  $\rho_o$  and  $T_o$ ) were reasonable, and were somewhat consistent with each others. The high temperature models ( $T_o = 2 \times 10^8$  K) show two distinctive regions in which the  $\dot{M}_{\text{out}} - \Gamma$  relation follows two different slopes. As mentioned earlier, the outflows found in the models with  $\Gamma \lesssim 1$  (Models 15, 16 and 17) are mainly thermally driven, but the models with  $\Gamma \gtrsim 1$  are mainly radiation-driven. The change in the main wind driving mechanism (from thermal pressure to radiation pressure) is the cause of the change in the strength or the slope of the  $\dot{M}_{\text{out}} - \Gamma$  correlation. The cause of the super-

Eddington accretion luminosity ( $\Gamma > 1$ ) will be discussed later in Section 4.1.

A simple power law ( $\dot{M}_{\text{out}} \propto \Gamma^q$ ) is used to fit the points for the models with radiation-driving dominated outflows, separately for each temperature. We find the power law indices ( $q$ ) as  $2.3 (\pm 0.3)$ ,  $1.8 (\pm 0.2)$  and  $1.8 (\pm 0.1)$  for  $T_o = 2 \times 10^6$ ,  $2 \times 10^7$  and  $2 \times 10^8$  K, respectively. These values are very similar to each others, i.e. the slope of the correlation is independent of or very insensitive to the outer boundary temperature. The slope for  $T_o = 2 \times 10^6$  K seems to be slightly higher than those of the higher temperature models; however, when the point corresponding to Model 2 ( $\rho_o = 2 \times 10^{-21}$  g cm $^{-3}$ ) is excluded from the line fit, we obtain the power law index  $q = 1.9$  which is in agreement with those of the models with the higher temperatures. We note that the outflow in Model 2 is relatively weak and it may not be entirely radiation-driven as its  $\Gamma$  is very close to that of Model 1, which does not produce an outflow.

The figure also shows the mass-loss rate predicted by the radiation-driven wind model of Castor et al. (1975) (CAK model) for a comparison. The CAK model predicts  $q = 1.67$  for  $\Gamma \ll 1$  and  $q \geq 2$  for  $\Gamma \lesssim 1$  which are very similar to the slopes found here. Their model assumes spherical symmetry, and the mass outflow rates becomes infinity as  $\Gamma$  approaches to 1. The differences between their model and our model are not only due to the assumed symmetries (spherical versus axial), but also in the implementation of the underlining luminosities. Our wind driving luminosity is coupled to the mass inflow/accretion rate of the system while their luminosity is fixed constant and they do not have inflows in their model.

Motivated by the insensitivity of the slope of  $\dot{M}_{\text{out}} - \Gamma$  curves on  $T_o$ , we compute the slope using the points from all three temperatures (excluding the thermally-driving dominated models and the lowest temperature models with  $\Gamma \gtrsim 1.5$ : Models 6, 7, 8, 9, 15, 16 and 17). The corresponding slope is found as  $2.0 (\pm 0.1)$ . A separate power law is applied to the points with four highest  $\Gamma$  (Models 6, 7, 8 and 9) in the  $T_o = 2 \times 10^6$  K models, and its index is  $0.1 (\pm 0.1)$ . For the models with the thermally driven outflows with  $T_o = 2 \times 10^8$  K (Models 15, 16 and 17), the power law index is  $0.4 (\pm 0.1)$ . Table 2 summarises the power law indices found in this analysis. We note that theoretical and numerical studies of radiation driven stellar and disc winds (e.g. Castor et al. 1975; Proga, Stone, & Drew 1998; Proga 1999) predict  $q \geq 1.67$ , which is quite close to the values found in this study.

When the outer boundary density  $\rho_o$  becomes too small ( $\rho_o \lesssim 1 \times 10^{-21}$  g cm $^{-3}$ ), as in Model 1, no outflow is formed for  $T_o = 2 \times 10^6$  K. Similarly, no outflow is found for the models with  $\rho_o \lesssim 4 \times 10^{-22}$  g cm $^{-3}$  as in Model 10, for  $T_o = 2 \times 10^7$  K. Unlike in the lower temperature models, an outflow forms for  $T_o = 2 \times 10^8$  K, even with a relatively small outer boundary density ( $\rho_o = 0.5 \times 10^{-22}$  g cm $^{-3}$ ). The minimum outer boundary density  $\rho_o^{\text{min}}$  or the minimum Eddington ratio  $\Gamma^{\text{min}}$  above which an outflow can be formed depends on the ambient temperature ( $T_o$ ). The higher the value of  $T_o$ , the smaller the value of  $\Gamma^{\text{min}}$ . For example,  $\Gamma^{\text{min}} \sim 0.3$ ,  $\sim 0.2$  and  $< 0.05$  for  $T_o = 2 \times 10^6$ ,  $2 \times 10^7$  and  $2 \times 10^8$  K, respectively. When the outer boundary temperature becomes higher, the average temperature of the gas in the temperature becomes also higher. This makes the gas to be driven thermally more easily; hence, the outflow starts to form even at lower value of  $\Gamma$ . Note that the Eddington ratio  $\Gamma$ , by definition, only considers the radiation force due to Thomson scattering. The radiation force considered here includes also line scattering process (see e.g. Paper I for our implementation of the radiation force); hence, the total radiation force could exceed the gravity even for  $\Gamma < 1$ .

The correlation between  $\dot{M}_{\text{out}}$  and  $\Gamma$  (for the radiation driven outflow cases) may continue for higher luminosities (i.e.  $\Gamma > 5$ ), but we are not able to confirm this due to a limitation of our code. Strong shocks form in the flows in the models with  $\Gamma > 5$  (for  $T_o = 2 \times 10^7$  and  $2 \times 10^8$  K models), and the code fails to handle them. Unfortunately, this prevents us from exploring models with very high accretion luminosities.

### 3.2 Time-Dependent Behaviours of Mass-Accretion Rates

Not all the models we consider here reach steady state solutions and have smooth inflows (and outflows). Some models do show variability in the mass-accretion rate ( $\dot{M}_a$ ) (the mass flux across the inner boundary of our computational domain). To quantify the degrees of variability, we compute the standard deviations of the time series values of  $\dot{M}_a$  and  $\Gamma$  for each model. The results are shown in Table 1. Further, to compare the amount of variability from different models more directly, we normalise the standard deviation by the time-averaged values of  $\dot{M}_a$ . In other words, we compute the ratio ( $\sigma_n$ ) of the standard deviation of  $\dot{M}_a$  to the time-averaged values of  $\dot{M}_a$ . The distribution of the normalised standard deviation  $\sigma_n$  is shown in Fig. 2. The figure shows  $\sigma_n$  as a function of  $\Gamma$  for Models 1–22 in Table 1.

We categorise the time-dependent natures of  $\dot{M}_a$  in our simulations into three types: (1) steady, (2) semi-steady and (3) spiky, based on the value  $\sigma_n$ . We define a model as *steady* when  $\sigma_n < 0.01$ , and as *semi-steady* when  $0.01 < \sigma_n < 1.0$ . Further, it is defined as *spiky* when  $\sigma_n > 1.0$ . Based on this definition, the variability type of each model is assigned and placed also in Table 1. Out of 22 models considered here, 6 are found as *steady*, and 13 as *semi-steady*. Only 3 models are found as *spiky*. Fig. 3 shows examples of the three different types of  $\dot{M}_a$  variability found in our simulations.

In the models with steady  $\dot{M}_a$ , inflows and outflows are smooth and the level of  $\dot{M}_a$  variability (the change with respect to the time averaged value of  $\dot{M}_a$ ) is typically less than 1 per cent. In the models with semi-steady  $\dot{M}_a$ , small-sized and relatively high density structures are occasionally formed in the flows, and some of them fall toward the centre. This causes moderate levels of variability ( $\lesssim 200$  per cent) in a relatively short timescale ( $\sim 10^{11}$  s). The models marked as *spiky* occurs only in the high temperature models ( $T_o = 2 \times 10^8$  K), and in the cases when the outflows is thermally driven. The relatively high temperature of gas keeps the sound speed to be high. As a result, the outflows in these models are sub-sonic. The effect of a small density perturbation in the flow that occurs near the inner boundary propagates through the entire computational space in relatively small timescale (because of the high sound speed) compared to the dynamical timescale of the flows. The acoustic wave generated near inner boundary propagates outward and bounces back at  $r = r_o$  in the hot media, when the outflow is relatively weak and when the radiative force is relatively weak. This causes rather stochastic sharp peaks and dips (spikes) in the  $\dot{M}_a$  variability curves. The level of variability is rather large ( $> 100$  per cent) in these models. We do not consider the models with spiky  $\dot{M}_a$  (i.e. Models 15, 16 and 17) as physical because they are affected by the inner boundary. The inner boundary is too far from the BH for the inflow to become supersonic in those cases; hence, it can reflect the flows and turn inflows into outflows.

When we exclude the unphysical spiky  $\dot{M}_a$  models (i.e. Models 15, 16 and 17) from Fig. 2, we find a very weak correlation between  $\sigma_n$  and  $\Gamma$ , i.e. the larger the accretion luminosity, the amount of variability tends to be larger. The distribution of  $\sigma_n$  seems to be

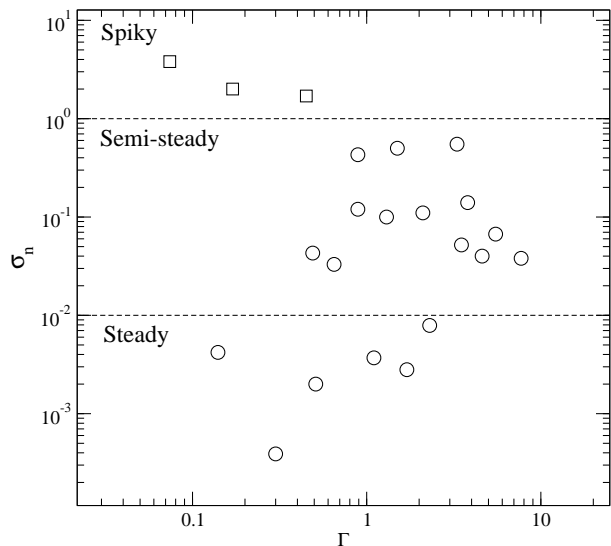


**Figure 2.** Distribution of the normalised standard deviation  $\sigma_n$  of the mass accretion rates computed at the inner boundary for Models 1–22 in Table 1 is shown as a function of the Eddington ratio  $\Gamma$ . Models are categorised as *steady*, *semi-steady* or *spiky* when  $\sigma_n < 0.01$ ,  $0.01 < \sigma_n < 1.0$  and  $\sigma_n > 1.0$ , respectively. The boundaries between different types are indicated by horizontal lines (*dashed line*). The models which belong to the *steady* and *semi-steady* types are indicated by *circles*, and those belong to the *spiky* are indicated by *squares*. A very weak correlation between  $\sigma_n$  and  $\Gamma$  is seen for the data points belong to the *steady* and *semi-steady* types.

continuous (as a function  $\Gamma$ ). There is no clear separation of the two populations: the *steady* and *semi-steady* types, according to the figure.

### 3.3 Disc Wind Like Solutions

In most of the models explored (Table 1), the flow morphology are quite similar to the ones presented earlier (Papers I, II and III) e.g. bipolar outflows and fragmented dense cold cloud outflows. Here we report a new morphological type of solutions which has not been seen in our previous models. Among the low temperature ( $T_o = 2 \times 10^6$ ) models, when the density at  $r = r_o$  is relatively high ( $\rho_o > 5.0 \times 10^{-20}$  g cm $^{-3}$ ), the flow starts to resemble a radiation driven disc wind which arises from the very inner part of accretion discs (e.g. Proga et al. 1998; Proga et al. 1999), and a thermally-driven disc wind which arises from relatively large radii (e.g. Woods et al. 1996; Proga & Kallman 2002).

Fig. 4 demonstrates how the wind configuration transforms to a disc wind like solution. For this purpose, we compare the gas flows from Models 5, 8 and 9 which have the same outer boundary temperature  $T_o = 2 \times 10^6$  K but have different values of  $\rho_o$ , i.e.  $1 \times 10^{-20}$ ,  $1 \times 10^{-19}$  and  $2 \times 10^{-19}$  g cm $^{-3}$ , respectively. In Model 5, which has the lowest  $\rho_o$  value among the three, the high density gas streams falling toward the centre in relatively wide range of polar angles ( $50^\circ \lesssim \theta < 90^\circ$ ). The outflow is formed only in the mid polar angles  $30^\circ \lesssim \theta \lesssim 50^\circ$ . When  $\rho_o$  is increased 10 times (Model 8), the infalling dense streams of gas seen in the previous model are converged toward equatorial plane, and form a relatively dense disc-like structure. The outflow now occurs at larger polar angles and in wider angle range ( $45^\circ \lesssim \theta \lesssim 80^\circ$ ). The outflow resembles a disc wind. However, the high density gas near  $r = r_o$  at lower polar angles  $\theta \lesssim 45^\circ$  prevents the gas from

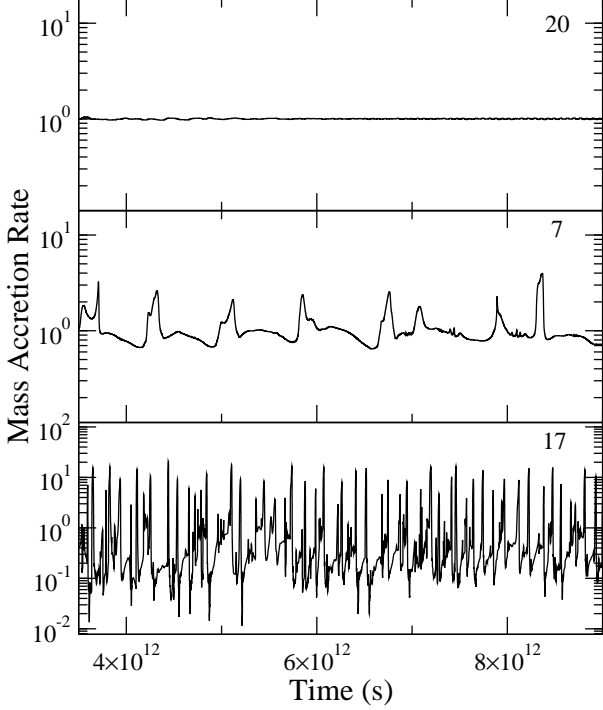


**Figure 3.** Examples of different types of time-dependent mass-accretion rate variability patterns. The panels show the mass-accretion rates as a function of time for selected samples of models which show steady (top), semi-steady (middle) and spiky (bottom) variabilities (see Table 1). The number on the upper right hand corner of each panel indicates the corresponding model number in Table 1. The mass accretion rates on the vertical axes are in units of the time-averaged mass accretion rate of each model which are  $39$ ,  $15$  and  $7.5 \times 10^{25} \text{ g s}^{-1}$  from the top to bottom panels, respectively.

forming outflows and keeps the gas relatively hot in the polar direction. In this case, no fast low-density polar wind is formed unlike the ones seen in the models of Proga et al. (1998). This difference is caused by the difference in the treatment of boundary conditions, i.e. in Proga et al. (1998), the density and temperature at  $r = r_o$  are unconstrained. When we increase the density  $\rho_o$  by a factor of 2 (Model 9), the radiative force becomes strong enough to push away the high density gas in the polar direction, and the fast low-density polar wind is formed. However, in this case, the outflowing mass-flux in the polar direction is negligible (due to its very low density) compared to the outflow in the higher polar angles ( $\theta \gtrsim 45^\circ$ ). The accretion region is now converged to a much thinner equatorial disc, and a very wide outflow ( $45^\circ \lesssim \theta \lesssim 85^\circ$ ) or a disc wind is formed.

The saturation of the mass outflow rates at the high  $\Gamma$  values for  $T_o = 2 \times 10^6 \text{ K}$  models seen in Fig. 1 (Section 2.4) can be explained qualitatively by the change of the outflow pattern to a disc wind like configuration. Before the saturation occurs, the polar outflow can become wider by squeezing the high density inflowing stream toward the equatorial regions. This allows the mass outflow rate to grow proportionally with the mass-accretion rate or with the accretion luminosity  $\Gamma$ . In the higher  $\Gamma$  models, e.g. Models 8 and 9, the dense inflowing gas streams are converged all the way to the equatorial plane ( $\theta \approx 90^\circ$ ); hence, the polar angle range, in which outflow occurs, can not be increased any more. This limit in the size of the outflow polar angle range is the cause of the saturation of the mass outflow rates (the flat part of the  $\dot{M}_a$ - $\Gamma$  relation in Fig. 1).

In addition, once the flow becomes disc-wind like, it is harder for a system to produce stronger outflows for the following reason. In our models, the radiation peaks in polar directions (cf.  $\cos \theta$  dependency of the radiation flux as in Sections 2.1 and 4.1); hence, the most of the radiation escapes in the polar direction. In the disc-wind like flow morphology, however, there is almost no gas to be blown away by the radiation in the polar regions (Fig. 4). This results in the insensitivity of the mass outflow rate with  $\Gamma$ . Near the equatorial plane where most of the infalling gas is concentrated, the radiation is very weak because of the  $\cos \theta$  dependency of the disc radiation, and because of the very high optical depth of the disc like structure. Finally, the temperature map for the disc-wind like solution shows that the temperature of the wind is relatively high ( $T \sim 10^7 \text{ K}$ ). This temperature is too high for the radiation force due to line processes (line force hereafter) to be effective. We confirmed that the main wind driving force for the wind in this case is the continuum radiation force (due to electron scattering).

## 4 DISCUSSIONS

### 4.1 Accretion with Super-Eddington Luminosity

Many of the self-consistently determined accretion luminosities in the models presented in Section 3.1 (see Table 1 and Fig. 1) are found to be above the Eddington luminosity ( $\Gamma > 1$ ). At first, this may be puzzling since one would expect that the high luminosity hence strong radiation pressure induced by the high mass accretion rate should regulate the amount of luminosity and keep  $\Gamma < 1$ . This might be the case if the gas were not rotating and the radiation were spherically symmetric; however, the situation changes when the source geometry of the strong UV radiation is not spherical. Because of the disc geometry, the flux of the disc radiation depends on the polar angle. It radiates more in the polar directions ( $\mathcal{F}_{\text{disc}} \propto |\cos \theta|$ ), as mentioned in Section 2.2, and it turns inflows into outflows. To see how this assumption leads to the super-Eddington accretion solutions found in our models, consider the ratios ( $\Gamma_\theta$ ) of the radial forces per unit mass (accelerations) by radiation ( $g_{\text{rad}}$ ) and gravity ( $g$ ) (cf. equation 2). To simplify our argument, we consider only the radiation force due to electron scattering and exclude that due to spectral line processes here. By setting  $\mathcal{M} = 0$  in equation 7, the radiative acceleration can be written as

$$g_{\text{rad}}^e = \frac{\sigma_e L}{4\pi r^2} (f_* + 2f_{\text{disc}} \cos \theta) \quad (10)$$

where  $\sigma_e$  and  $L$  are the electron scattering cross section and the total accretion luminosity respectively. The superscript  $e$  on the left term indicates that the acceleration is only due to electron scattering. The fractional luminosities of the X-ray emitting spherical region and that of the UV emitting accretion are assumed to be  $f_* = 0.05$  and  $f_{\text{disc}} = 0.95$  (Section 2.1). Using equation 10 and the gravitational acceleration  $g = -GM_{\text{BH}}/r^2$  (assuming it is Newtonian and a point-mass), the ratio becomes

$$\Gamma_\theta = \left| \frac{g_{\text{rad}}^e}{g} \right| = \Gamma (f_* + 2f_{\text{disc}} \cos \theta) \quad (11)$$

where  $\Gamma = \sigma_e L / (4\pi GM_{\text{BH}})$  and is the Eddington ratio. Fig. 5 shows the values of  $\Gamma_\theta$  plotted as a function of the polar angle  $\theta$  for a range of the Eddington ratios ( $0.1 < \Gamma < 10$ ). We consider only the radiation force due to electron scattering. Therefore, the lines shown in the figure are only lower limits of  $\Gamma_\theta$  values for at a given  $\theta$  angle. The figure shows  $\Gamma_\theta < 1$  (the outward radiation force is smaller than the inward gravitation force) at all  $\theta$  for  $\Gamma < 0.5$  cases.

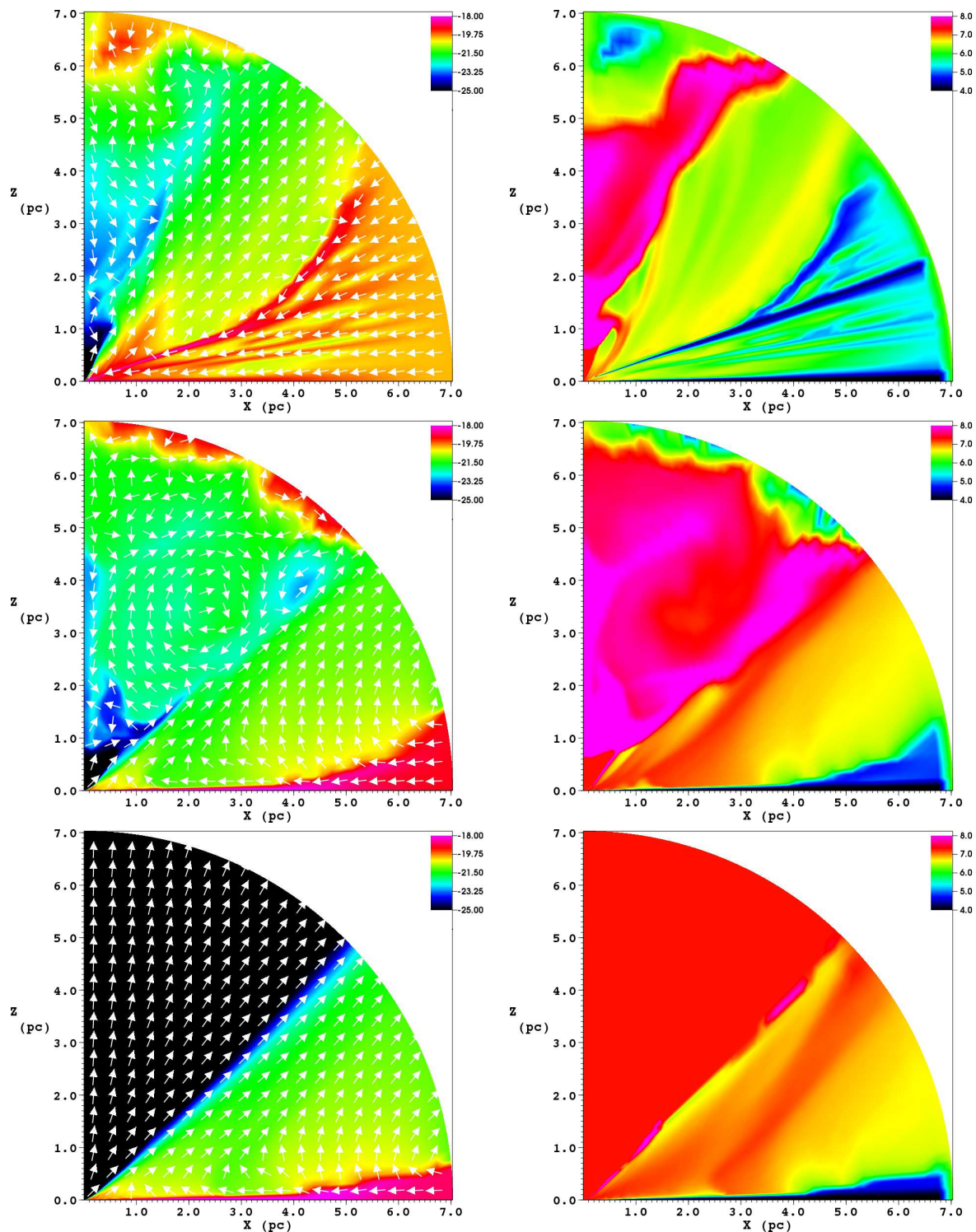


**Figure 4.** A transition to a disc-wind like solution in the low temperature models ( $T_0 = 2 \times 10^6$  K). The density (in logarithmic scale) over-plotted with the directions of poloidal velocity as arrows (*left column*) for Models 5 (*top*), 8 (*middle*) and 9 (*bottom*) are shown. The figures are placed in order of increasing density at  $r = r_0$  ( $\rho_0$ ), from the top to bottom (cf. Table 1). The corresponding temperature maps (in logarithmic scale) of each model are placed in the *right column*. The colour tables for the density and temperature maps are labelled with the logarithmic values in  $\text{g cm}^{-3}$  and K, respectively. The top density plot shows the high density gas streams falling toward the centre in the wide range of polar angles ( $\theta \gtrsim 50^\circ$ ), and the outflow is formed only in the mid polar angles  $30^\circ \lesssim \theta \lesssim 50^\circ$ . The middle density plot shows the infalling dense gas forming a relatively thick disc-like structure, and the outflow occurs in larger and wider polar angles ( $45^\circ \lesssim \theta \lesssim 80^\circ$ ) which resembles a disc wind (e.g. Proga et al. 1998). The high density gas near  $r = r_0$  at lower polar angles ( $\theta \lesssim 45^\circ$ ) prevents the gas from forming outflows in the polar direction. The bottom density plot shows the accretion region is now squeezed to a much thinner equatorial disc, and a very wide outflows ( $45^\circ \lesssim \theta \lesssim 85^\circ$ ) or a disc wind is formed.

For the models with  $\Gamma > 1$ , the figure shows that  $\Gamma_\theta$  can still be less than 1 at larger values of  $\theta$ . For example, for  $\Gamma = 5$  model,  $\Gamma_\theta$  is still smaller than 1 for  $\theta \gtrsim 85^\circ$ , and for  $\Gamma = 10$  case,  $\theta \gtrsim 88^\circ$ . This critical angle  $\theta_{\text{crit}}$  at which the radiation force equals the gravity ( $\Gamma_\theta = 1$ ) becomes larger as the accretion luminosity or  $\Gamma$  increases. The inflow of gas is potentially possible only in the polar angle range which has  $\Gamma_\theta < 1$ . Therefore, the location of the accretion streams becomes closer and closer to the equatorial plane. The most important point of Fig. 5 for us is that  $\Gamma_\theta$  can be still less than 1 near the equatorial plane which allows an accretion of gas in a super-Eddington luminosity environment. This is a direct consequence of the disc geometry which allows most of the radiation to escape in polar direction, but not in the equatorial direction. In addition, the radiative cooling in the dense gas confined near the equatorial plane is very efficient, and the gas temperature is kept low (e.g. see the bottom panels of Fig. 4). This also helps to accrete the matter in the equatorial plane.

Interestingly, a recent 3-D radiation-hydrodynamic simulation of the formation of a massive (stellar) binary by accretion by Krumholz et al. (2009) demonstrated that the radiation pressure would not be able to halt accretion totally even at  $\Gamma > 1$  because of gravitational and Rayleigh Taylor instabilities which channel the accretion of matter on to the binary from the accretion disc, and the self-shielding of radiation by high density gas filaments which could still experience a net inward force. Note that this type of self-shielding does not occur in our model since the UV radiation, which causes 95 per cent or more of the total radiation force in our model, is assumed to be optically thin in our flows.

#### 4.2 Effect of Luminosity Limit

The self-consistent accretion luminosity models presented in Section 3.1 do not limit their luminosities to be below the Eddington luminosity (i.e.  $\Gamma < 1$ ) as explained above. A super-Eddington or super-critical accretion on the SMBH may be possible (e.g. Jaroszynski et al. 1980; Abramowicz, Calvani, & Nobili 1980; Begelman 2002; Ohsuga et al. 2002; Ohsuga et al. 2005; see also a review by Abramowicz 2005.). However, we can not be certain whether the accretion disc would be still stable and would accrete at a such high Eddington ratio (e.g.  $\Gamma = 3.3$  for Model 14) because we do not model the dynamical evolution of the accretion disc itself (cf. Section 2.5). When the accretion disc becomes optically thick, the radiation field of the interior of the disc itself is expected to become very isotropic. In general, a super-Eddington accretion in such environment is much more difficult than the one we considered in this paper. When the radiation field is isotropic, one would expect the accreting gas to be turned around when  $\Gamma > 1$  and the disc becomes optically thick; hence, it would tend to keep the mass-accretion rate below the super-Eddington rate. For this reason, we examine the possibility that the accretion luminosity is limited to the Eddington luminosity, and study the consequences of such a limit.

We recomputed the models with the self-consistent evaluation of the accretion luminosity, but now the upper limit of the accretion luminosity is set to the Eddington luminosity. Fig. 6 shows the mass outflow rates at  $r = r_o$  plotted against the mass accretion rates at the inner boundary for the models with  $T_o = 2 \times 10^7$  K with and without the upper limit on the luminosity. Only the models with high mass accretion rates (near and above the mass accretion rate corresponding to  $\Gamma = 1$ ) are shown in the figure (cf. Table 1). The figure is similar to Fig. 1, but the mass accretion rate is used for the horizontal axis instead of  $\Gamma$ . The figure shows that mass out-

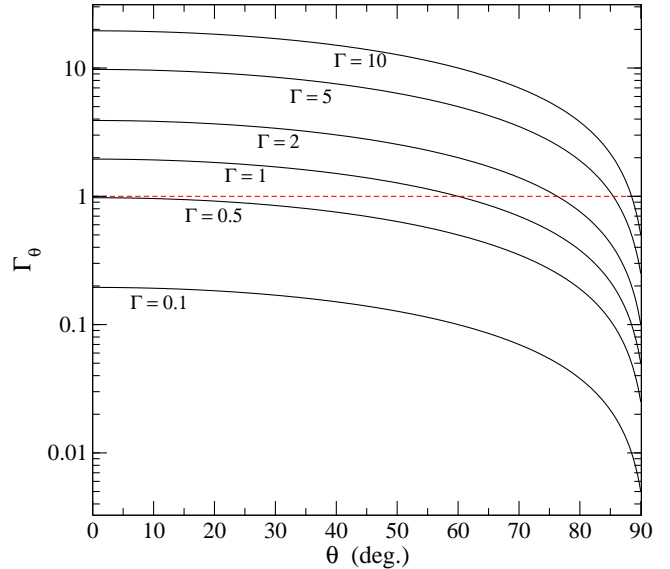


**Figure 5.** Ratios ( $\Gamma_\theta$ ) of the radiation force due to electron scattering ( $g_{\text{rad}}^e$ ) to the gravitational force ( $g$ ) as a function of spatial polar angle  $\theta$  for different values of the Eddington ratios  $\Gamma$  (solid lines). The lines indicate the lower limit of the ratio because the radiation force due to line process are not included here. The horizontal dashed line indicates  $\Gamma_\theta = 1$  at which the magnitudes of radiation force and the gravitational force are equal. In the polar angle ranges below the  $\Gamma_\theta = 1$  line, an inflow of gas is possible. This range decreases as  $\Gamma$  becomes larger, indicating that an inflow can occur in larger polar angles, i.e. closer to the equatorial planes. Note that even for  $\Gamma = 5$ ,  $\Gamma_\theta$  is still smaller than 1 for  $\theta \gtrsim 85^\circ$ , and for  $\Gamma = 10$  case,  $\theta \gtrsim 88^\circ$ . The fractional luminosities of the spherical X-ray emission and that of the disc UV emission are assumed to be 0.05 and 0.95 respectively (cf. Section 2.1).

flow weakens (the mass outflow rate decreases) for the models with larger mass accretion rates (larger than the value corresponding to  $\Gamma = 1$ ). On the other hand, the models with smaller mass accretion rates (below  $\Gamma = 1$  line in the figure) have nearly identical mass outflow rates. This behaviour is expected from the luminosity limiting model. The models with higher mass accretion rates are affected by the luminosity limit hence have smaller luminosities compared to the cases without the limit. A smaller luminosity naturally leads to a lower mass outflow rate. Interestingly this decrease or the saturation of the outflow strength (the mass outflow rates) is very similar to that one seen in the high  $\Gamma$  end of the low temperature models ( $T_o = 2 \times 10^6$  K) in Section 3.1 (see Fig. 1) although the physical reason for the cause of the saturation is different.

#### 4.3 Effect of unconstraining the outer boundary temperature

Motivated by the insensitivity of the slopes of  $\dot{M}_{\text{out}}-\Gamma$  relations on the outer boundary temperature ( $T_o$ ) found in Section 3.1, we now investigate the effect of allowing the temperature at  $r_o$  to be computed self-consistently instead of being fixed at some predetermined value. The models presented so far have assumed that the gas which surrounds our computational domain is ‘Comptonised’ at a constant temperature  $T_o$ . Here, we consider 7 additional models in which we do not constrain the temperatures at  $r = r_o$ . We now compute the temperatures self-consistently by solving the equation of the energy (i.e., equation 3) at  $r_o$ , as it is

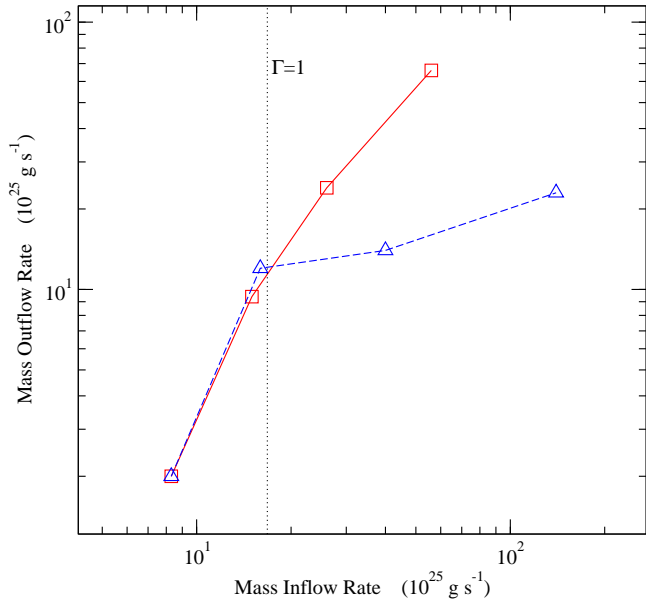


**Figure 6.** Effect of limiting accretion luminosity on the mass outflow rates for the models with the ambient temperature  $T_o = 2 \times 10^7$  K. The mass outflow rates are plotted against the mass inflow rates for the models with (triangles) and without (squares) the threshold accretion luminosity for a comparison. For the models with the luminosity limit, the maximum allowed luminosity is set to the Eddington luminosity, i.e.  $\Gamma = 1$ . The mass inflow rate that corresponds to  $\Gamma = 1$  is indicated by a vertical dotted line.

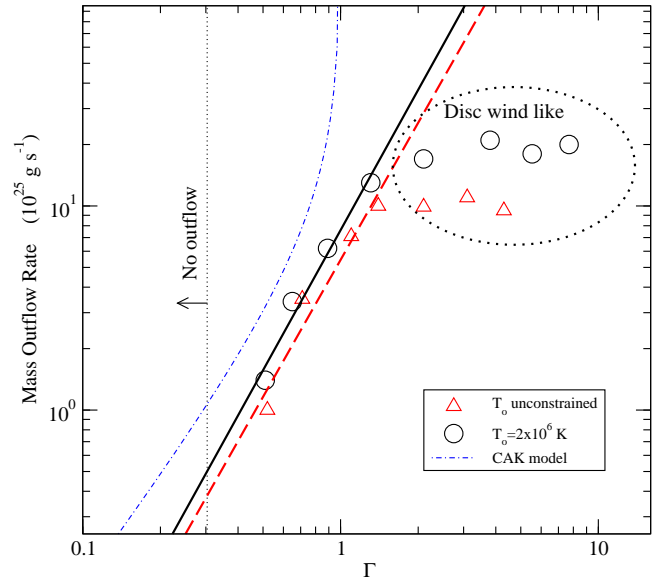
done for any other points in our computational domain. The basic model parameters and results are summarised in Table 3.

Fig. 7 shows the mass outflow rates ( $\dot{M}_{\text{out}}$  through the outer boundary) plotted as a function of the Eddington ratio ( $\Gamma$ ) for the new runs, along with those of the models with  $T_o = 2 \times 10^6$  K from Section 3.1 (see also Table 1). Both sets of the models show a very similar dependency of  $\dot{M}_{\text{out}}$  on  $\Gamma$ . This is mainly because the average temperatures (self-consistently determined) at  $r_o$  for the new models considered here are relatively low and similar to that of the fixed outer boundary temperature models i.e.  $T_o = 2 \times 10^6$  K. Table 3 lists the average outer boundary temperatures for the individual runs.

A strong correlation between  $\dot{M}_{\text{out}}$  and  $\Gamma$  is found for the models with  $\Gamma \lesssim 2$ . The new set of models also show a saturation of  $\dot{M}_{\text{out}}$  beyond  $\Gamma \gtrsim 2$  as in the  $T_o = 2 \times 10^6$  K (fixed) models, and exhibit the disc wind like solutions (cf. Section 3.3). We applied a simple power-law fit for the points with  $\Gamma \lesssim 2$  (Models 28, 29, 30 and 31 in Table 3), and found its index as  $q = 2.2 \pm 0.4$  which is very similar to that of the  $T_o = 2 \times 10^6$  K models and that of the CAK stellar wind model (cf. Table 2). No outflow was found for the models with  $\Gamma \lesssim 0.3$ .

The self-consistently determined temperatures at  $r = r_o$  in the new models depend on the polar angle. In general, the temperature decreases from  $\sim 10^7$  K in the polar direction ( $\theta = 0$ ) to  $\sim 10^4$  K as  $\theta$  increases toward the equatorial plane. At the higher polar angles ( $\theta \gtrsim 50^\circ$ ), relatively high density accretion streams are present. The high density columns of accreting gas have high optical depths; hence, they are very efficient for shielding the strong ionization radiation from the central source. This causes the lower temperatures at  $r = r_o$  for the higher  $\theta$  values.

In summary, the inflow and outflow properties for the new models are very similar to those of the low outer boundary tem-



**Figure 7.** Comparison of models with (circles) and without (triangles) fixing the temperature at the outer boundary ( $T_o$ ). The mass outflow rates ( $\dot{M}_{\text{out}}$  through the outer boundary) are plotted as a function of the Eddington ratio ( $\Gamma$ ) for the models with  $T_o = 2 \times 10^6$  K from Section 3.1 (see Table 1) and for the new models without  $T_o$  constrained (see Table 3). Both sets of the models show a very similar dependency of  $\dot{M}_{\text{out}}$  on  $\Gamma$ . The models show strong correlations between  $\dot{M}_{\text{out}}$  and  $\Gamma$  when  $\Gamma \lesssim 2$ . The new set of models also show a saturation of  $\dot{M}_{\text{out}}$  beyond  $\Gamma \gtrsim 2$  as in the  $T_o = 2 \times 10^6$  K (fixed) models, and exhibit the disc wind like solutions (see Section 3.3). A simple power law is used to fit the points with  $\Gamma \lesssim 2$  (Models 28, 29, 30 and 31 in Table 3) which show a strong correlation between  $\dot{M}_{\text{out}}$  and  $\Gamma$ . The index of the power law fit for the new models is  $q = 2.2 \pm 0.4$  which is very similar to that of the  $T_o = 2 \times 10^6$  K models (see Table 2). The mass-loss rate predicted by the radiation-driven stellar wind model (CAK model) is also shown for a comparison (dash-dot line). The vertical line at  $\Gamma \approx 0.3$  (dotted line) indicates the approximate  $\Gamma$  value below which a model does not produce outflows.

perature models ( $T_o = 2 \times 10^6$  K). The disc wind like solutions also appear for the models with high accretion rates ( $\Gamma \gtrsim 2$ ).

#### 4.4 Assumption of flows with optically-thin UV radiation

As briefly mentioned in Section 2.1, our model takes into account for the attenuation of X-ray radiation by computing X-ray optical depth when computing the radiative cooling/heating rate and radiation forces; however, we assume that the flow is optically thin in UV. The attenuation of the UV radiation is not considered here because our model uses the method described by Stevens & Kallman (1990) who parametrised the line force by the photoionization parameter  $\xi$ . This simplification speeds up our calculation tremendously since  $\xi$  can be estimated rather quickly without computing the detail ionization levels of the gas. The formulation of Stevens & Kallman (1990) assumes that the UV radiation is optically thin; therefore, to be consistent with their original model, our model must make the same assumption.

We have checked the radial UV optical depths (between the inner and outer boundaries) of a several representative models (especially for those with high mass accretion rates,  $\Gamma > 1$ ) at a few time slices. For each case, the optical depths ( $\tau$ ) have been computed along each polar angle ( $\theta$ ). We found that  $\tau$  in general increases as  $\theta$

**Table 3.** Summary of models without  $T_o$  constrained

Model	$\rho_o$ ( $10^{-21}$ g cm $^{-3}$ )	$\dot{M}_{in}(r_i)$ ( $10^{25}$ g s $^{-1}$ )	$\Gamma$ ...	$\dot{M}_{out}(r_o)$ ( $10^{25}$ g s $^{-1}$ )	$T_{ave}^\dagger$ ( $10^6$ K)	Variability ...	Outflow Morphology ...
28	10	8.9(0.68) $^\ddagger$	0.52(0.04) $^\ddagger$	1.0(0.032) $^\ddagger$	1.4	semi-steady	wide polar
29	20	12(0.58)	0.71(0.034)	3.5(0.52)	1.4	semi-steady	wide polar
30	40	18(1.1)	1.1(0.1)	7.1(1.4)	3.6	semi-steady	wide polar
31	80	25(2.6)	1.4(0.2)	10(2.3)	8.0	semi-steady	wide polar
32	160	36(4.9)	2.1(0.3)	9.9(2.6)	9.8	semi-steady	disc-wind like
33	320	52(2.6)	3.1(0.2)	11(0.48)	8.5	semi-steady	disc-wind like
34	640	72(0.56)	4.3(0.03)	9.5(0.19)	13	steady	disc-wind like

( $\dagger$ ) Self-consistently determined average temperatures at the outer boundary

( $\ddagger$ ) Values in brackets are the standard deviations of the time series values.

increase. The optical depth in polar directions ( $\theta \lesssim 60^\circ$ ) are almost always less than 0.1. Even at larger polar angles ( $60^\circ \lesssim \theta \lesssim 85^\circ$ ),  $\tau < 1$ . Only along a couple of  $\theta$  angles near the equator ( $\sim 90^\circ$ ) where the relatively high density gas is prominent (c.f. Fig. 4),  $\tau$  becomes greater than 1. From this analysis, we conclude that our assumption of optically thin UV radiation in our model is reasonable. Since the input radiation field in our model becomes smaller as  $\theta$  increases (c.f. equation 7) and it becomes very small along the equator, the effect of the small optical depths at larger  $\theta$  angles found here is minimal. On the other hand, if the angular distribution of the radiation field peaks in the equatorial direction, then the UV optical depths found here would make some effect on our results; however, this is not the case considered in this work.

If, however, the optical depth becomes very large ( $\tau \gg 1$ ) in the polar region in which our input radiation field is strongest, we would need to consider the effect of attenuation and scattering of the photons (see e.g. Ostriker, McKee, & Klein 1991; Murray et al. 1994; Ohsuga et al. 2005). In particular, the scattered photons from the polar region to equatorial region would redistribute the angular distribution of our input radiation field. Furthermore, the scattered photons would heat up the relatively low temperature accreting gas near the equator (c.f. Fig. 4). This would especially change the scale height of the ‘disc-like’ accretion structure, and the corresponding mass-accretion rate. To include the effect of multiple scattering of photons, one would need a proper treatment of radiative transfer. Implementing such an effect in our model would require a major change in our computational code, and this is beyond the scope of this paper.

## 5 CONCLUSIONS

We have performed a set of 2-D (axisymmetric) hydrodynamical simulations (Table 1) to study radiation-driven outflows from a central part ( $\lesssim 10$  pc) of AGN. We have extended the radiation-driven AGN outflow model of Proga (2007) by relaxing the assumption of a constant accretion luminosity. This allows us to determine the accretion luminosity consistently with the mass accretion rate at the inner boundary, and consequently the two quantities are coupled through the radiation field. Therefore, we made another step toward a more comprehensive self-consistent hydrodynamical models with radiative feedback. Although the accretion luminosity is self-consistently determined in our model, the angular distribution of the radiation field is not self-consistently determined, but it is fixed while simulations proceed. The radiation always peaks in the polar direction and decreases significantly in the equatorial direction.

We have examined the dependency of mass outflow rates on the accretion luminosity (Section 3.1) for three different outer boundary temperatures ( $T_o = 2 \times 10^6$ ,  $2 \times 10^7$  and  $2 \times 10^8$  K) by varying the outer boundary density ( $\rho_o$ ). In the following, we summarise our main findings.

We found a relatively strong correlation between the mass outflow rates  $\dot{M}_{out}$  at the outer boundary ( $r = r_o$ ) and the Eddington ratio  $\Gamma$  (Fig. 1). The outflows found in our models can be divided into three groups: 1. thermally-driven winds, 2. radiation-driven winds with a wide inflow, and 3. radiation-driven wind with a narrow equatorial inflow (disc-wind like solutions). Out of 22 models considered here, the majority of them (19 models) produces radiation-driven outflow/winds (Groups 2 and 3). Only 3 models produce thermally driven winds (Group 2: Models 15, 16 and 17). The thermally driven winds are found only in the highest temperature models ( $T_o = 2 \times 10^8$  K). The disc-wind like outflows are found in 4 cases (Group 3: Models 6, 7, 8 and 9) which all have the lowest temperature at  $r = r_o$  ( $T_o = 2 \times 10^6$  K). No outflow is found for the models with  $\Gamma \lesssim 0.3$  when the ambient temperature is  $T_o = 2 \times 10^6$  K, and for the models with  $\Gamma \lesssim 0.2$  when  $T_o = 2 \times 10^7$  K.

For the models with radiation-driven outflows, we found that the correlation between  $\dot{M}_{out}$  and  $\Gamma$  can be described as a power law. The slope of the index of the power law ( $q$ ) is relatively insensitive to the outer boundary temperature  $T_o$  (Table 2). Using the models from all three values of  $T_o$  (see above), the index of the power law is found as  $q = 2.0 (\pm 0.1)$ . This is very similar to those of the radiation-driven stellar wind (e.g. Castor et al. 1975) and disc wind (e.g. Proga et al. 1998; Proga 1999) which predict  $q \geq 1.67$ . This confirms that a very similar power-law scaling of mass outflow rates with the luminosity of the continuum source works at extremely different mass regimes, namely  $M_* \sim 1 M_\odot$  (cataclysmic variables),  $\sim 10 M_\odot$  (massive stars) and  $\sim 10^8 M_\odot$  (AGN), which also have different types of spectral energy distributions and the geometry of the radiation field.

As in Papers I, II, and III, we find that the outflow is driven from an inflow. However, here we found cases of the inflow-outflow solution of an extreme form (Section 3.3) for the lowest outer boundary temperature models ( $T_o = 2 \times 10^6$  K) but with relatively high outer boundary densities ( $\rho_o \gtrsim 2 \times 10^{-20}$  g cm $^{-3}$ ). In these models, the inflow occur in a narrow zone near the equatorial plane which resembles a thin accretion disc, and the outflow occurs in a wide polar angles ( $0 < \theta \lesssim 85^\circ$ ). This type of the flow is very similar to a wind driven by radiation from a luminous accretion disc (e.g. Proga et al. 1998; Proga 1999; Proga & Kallman 2002). In our models, the inflowing gas is very slowly rotating, so that the rotation velocity of the inflowing disc-like structure is

much smaller than the Keplerian velocity. The outflows arise from the disc-like structure near the equatorial plane in a wide range of the radii ( $1.4 \times 10^{-2} \text{ pc} \lesssim r \lesssim 7 \text{ pc}$ ).

For the models with a relatively high density set at  $r = r_o$ , a system reaches a steady state at  $\Gamma > 1$  (see Table 1 and Fig. 1). In other words, we find the models can still accrete matter even with a super-Eddington luminosity (up to  $\Gamma \sim 4$ ). This is a multi-dimensional effect. In our axi-symmetric model, the radiation field or the strength of the radiation force is not spherically symmetric but has the  $\cos \theta$  dependency (equation 10). This allows gas to accrete near the equatorial plane even with a super-Eddington luminosity ( $\Gamma > 1$ ), as demonstrated in Fig. 5. Based on this figure, the correlation between  $\dot{M}_{\text{out}}$  and  $\Gamma$  (for the radiation driven outflow cases) is expected to continue up to  $\Gamma \sim 10$ ; however, we are not able to confirm this due to numerical difficulties in handling very strong shocks that occur in the flows in the models with  $\Gamma > 5$  (for  $T_o = 2 \times 10^7$  and  $2 \times 10^8$  K models). In the range of  $\Gamma$  values we have explored, we do not observe a complete shutdown of the accretion flow even at a super-Eddington luminosity, which is expected in a spherically symmetric model. The accretion is still self-regulating, but not as a spherical model predicts.

When we relax the assumption of a constant temperature at the outer boundary and self-consistently determine the temperatures there, the  $\dot{M}_{\text{out}}-\Gamma$  relation becomes very similar to that of the models with the lowest outer boundary temperature,  $T_o = 2 \times 10^6$  K (Fig. 7). The high accretion rate models ( $\Gamma \gtrsim 2$ ) show disc wind like solutions, as seen in the high accretion rate models with  $T_o = 2 \times 10^6$  K (Section 3.3).

The following is a list of some steps for our model that shall be considered in the future: (i) include the effect of scattered photons which might enhance heating of the cold equatorial inflow, (ii) adjust the continuum spectral energy distribution based on the mass and the luminosity of the system, and (iii) extend the computational domain up to a few 100 pc scale to capture the gas dynamics in the narrow line regions of AGN, and (iv) include dust.

In addition, we shall incorporate the results from smaller scale simulations (e.g. disc-wind models by Proga 1999) since not all the gas which accretes though our inner boundary (which is relatively large i.e.  $r = 0.014$  pc) would reach the central SMBH due to the wind from the accretion disc.

## ACKNOWLEDGEMENTS

Authors thank the anonymous referee for constructive comments and suggestions for improving the clarity of the manuscript. We thank Prof. J. Ostriker for very helpful discussion and comments. This work was supported by NASA through grant HST-AR-11276 from the Space Telescope Science Institute, which is operated by the Association of Universities for Research in Astronomy, Inc., under NASA contract NAS5-26555. A significant fraction of our simulations were performed on a SUN computer system funded by President of UNLV, D. B. Ashley through an Infrastructure Award to the Astronomy Group at UNLV. This work was also supported by the National Center for Supercomputing Applications under AST070036N which granted the accesses to the Intel 64 Linux Cluster Abe. Authors are grateful for the original developers of ZEUS-MP for making the code publicly available.

## REFERENCES

- Abramowicz M. A., Calvani M., Nobili L., 1980, *ApJ*, 242, 772  
 Abramowicz M. A., 2005, in Merloni A., Nayakshin S., Sunyaev R. A., eds., *Growing Black Holes: Accretion in a Cosmological Context*, Springer, Berlin, p. 257  
 Begelman M., de Kool M., Sikora M., 1991, *ApJ*, 382, 416  
 Begelman M. C., 2002, *ApJ*, 568, L97  
 Begelman M. C., Nath B. B., 2005, *MNRAS*, 361, 1387  
 Binney J., Tabor G., 1995, *MNRAS*, 276, 663  
 Blandford R. D., Payne D. G., 1982, *MNRAS*, 199, 883  
 Bondi H., 1952, *MNRAS*, 112, 195  
 Bottorff M., Korista K. T., Shlosman I., Blandford R. D., 1997, *ApJ*, 479, 200  
 Brighenti F., Mathews W. G., 2006, *ApJ*, 643, 120  
 Castor J. I., 1970, *MNRAS*, 149, 111  
 Castor J. I., Abbott D. C., Klein R. I., 1975, *ApJ*, 195, 157  
 Chartas G., Brandt W. N., Gallagher S. C., 2003, *ApJ*, 595, 85  
 Ciotti L., Ostriker J. P., 1997, *ApJ*, 487, L105  
 Ciotti L., Ostriker J. P., 2001, *ApJ*, 551, 131  
 Ciotti L., Ostriker J. P., 2007, *ApJ*, 665, 1038  
 Ciotti L., Ostriker J. P., Proga D., preprint (astro-ph/0901.1089)  
 Clarke D. A., 1996, *ApJ*, 457, 291  
 Crenshaw D. M., Kraemer S. B., George I. M., 2003, *ARA&A*, 41, 117  
 Dalla Vecchia C., Bower R. G., Theuns T., Balogh M. L., Mazzotta P., Frenk C. S., 2004, *MNRAS*, 355, 995  
 Di Matteo T., Springel V., Hernquist L., 2005, *Nature*, 433, 604  
 Dorodnitsyn A., Kallman T., Proga D., 2008a, *ApJ*, 675, L5  
 Dorodnitsyn A., Kallman T., Proga D., 2008b, *ApJ*, 687, 97  
 Emmering R. T., Blandford R. D., Shlosman I., 1992, *ApJ*, 385, 460  
 Everett J. E., Murray N., 2007, *ApJ*, 656, 93  
 Fabian A. C., Sanders J. S., Taylor G. B., Allen S. W., Crawford C. S., Johnstone R. M., Iwasawa K., 2006, *MNRAS*, 366, 417  
 Fontanot F., Monaco P., Cristiani S., Tozzi P., 2006, *MNRAS*, 373, 1173  
 Guo F., Oh S. P., Ruszkowski M., 2008, *ApJ*, 688, 859  
 Hamann F., Ferland G., 1992, *ApJ*, 391, L53  
 Hamann F., Kaplan K. F., Hidalgo P. R., Prochaska J. X., Herbert-Fort S., 2008, *MNRAS*, 391, L39  
 Hardee P. E., Clarke D. A., 1992, *ApJ*, 400, L9  
 Hayes J. C., Norman M. L., Fiedler R. A., Bordner J. O., Li P. S., Clark S. E., ud-Doula A., Mac Low M.-M., 2006, *ApJS*, 165, 188  
 Hopkins P. F., Hernquist L., Cox T. J., Di Matteo T., Martini P., Robertson B., Springel V., 2005, *ApJ*, 630, 705  
 Jaroszynski M., Abramowicz M. A., Paczynski B., 1980, *Acta Astronomica*, 30, 1  
 Kato Y., 2007, *Ap&SS*, 307, 11  
 Kato Y., Mineshige S., Shibata K., 2004, *ApJ*, 605, 307  
 Kim M., Ho L. C., Im M., 2006, *ApJ*, 642, 702  
 King A., 2003, *ApJ*, 596, L27  
 Königl A., Kartje J. F., 1994, *ApJ*, 434, 446  
 Krumholz M. R., Klein R. I., McKee C. F. and Offner S. S. R., Cunningham A. J., preprint (astro-ph/0901.3157)  
 Kurosawa R., Proga D., 2008, *ApJ*, 674, 97  
 Kurosawa R., Proga D., 2009, *ApJ*, 693, 1929 (Paper III)  
 Li H., Lovelace R. V. E., Finn J. M., Colgate S. A., 2001, *ApJ*, 561, 915  
 Lovelace R. V. E., Wang J. C. L., Sulkanen M. E., 1987, *ApJ*, 315, 504

- Lucy L. B., 1971, *ApJ*, 163, 95  
Lynden-Bell D., 1996, *MNRAS*, 279, 389  
Lynden-Bell D., 2003, *MNRAS*, 341  
Maloney P. R., 1999, *Ap&SS*, 266, 207  
McNamara B. R., Nulsen P. E. J., 2007, *ARA&A*, 45, 117  
McNamara B. R., Nulsen P. E. J., Wise M. W., Rafferty D. A., Carilli C., Sarazin C. L., Blanton E. L., 2005, *Nature*, 433, 45  
Murray N., Chiang J., Grossman S. A., Voit G. M., 1995, *ApJ*, 451, 498  
Murray N., Quataert E., Thompson T. A., 2005, *ApJ*, 618, 569  
Murray S. D., Castor J. I., Klein R. I., McKee C. F., 1994, *ApJ*, 435, 631  
Nakamura M., Li H., Li S., 2006, *ApJ*, 652, 1059  
Ohsuga K., 2007, *ApJ*, 659, 205  
Ohsuga K., Mineshige S., Mori M., Umemura M., 2002, *ApJ*, 574, 315  
Ohsuga K., Mori M., Nakamoto T., Mineshige S., 2005, *ApJ*, 628, 368  
Ostriker E. C., McKee C. F., Klein R. I., 1991, *ApJ*, 377, 593  
Proga D., 1999, *MNRAS*, 304, 938  
Proga D., 2003, *ApJ*, 585, 406  
Proga D., 2007, *ApJ*, 661, 693 (Paper I)  
Proga D., Begelman M. C., 2003, *ApJ*, 592, 767  
Proga D., Kallman T. R., 2002, *ApJ*, 565, 455  
Proga D., Kallman T. R., 2004, *ApJ*, 616, 688  
Proga D., Ostriker J. P., Kurosawa R., 2008, *ApJ*, 676, 101 (Paper II)  
Proga D., Stone J. M., Drew J. E., 1998, *MNRAS*, 295, 595  
Proga D., Stone J. M., Drew J. E., 1999, *MNRAS*, 310, 476  
Proga D., Stone J. M., Kallman T. R., 2000, *ApJ*, 543, 686  
Quilis V., Bower R. G., Balogh M. L., 2001, *MNRAS*, 328, 1091  
Rafferty D. A., McNamara B. R., Nulsen P. E. J., 2008, *ApJ*, 687, 899  
Rafferty D. A., McNamara B. R., Nulsen P. E. J., Wise M. W., 2006, *ApJ*, 652, 216  
Rybicki G. B., Hummer D. G., 1978, *ApJ*, 219, 654  
Sazonov S. Y., Ostriker J. P., Ciotti L., Sunyaev R. A., 2005, *MNRAS*, 358, 168  
Scannapieco E., Silk J., Bouwens R., 2005, *ApJ*, 635, L13  
Schawinski K. et al., 2009a, *ApJ*, 690, 1672  
Schawinski K., Virani S., Simmons B., Urry C. M., Treister E., Kaviraj S., Kushkuley B., 2009b, preprint (astro-ph/0811.3970)  
Shakura N. I., Sunyaev R. A., 1973, *A&A*, 24, 337  
Soker N., Pizzolato F., 2005, *ApJ*, 622, 847  
Sobolev V. V., 1957, *Soviet Astronomy*, 1, 678  
Springel V., Di Matteo T., Hernquist L., 2005a, *ApJ*, 620, L79  
Springel V., Di Matteo T., Hernquist L., 2005b, *MNRAS*, 361, 776  
Stevens I. R., Kallman T. R., 1990, *ApJ*, 365, 321  
Stone J. M., Norman M. L., 1992, *ApJS*, 80, 753  
Tremonti C. A., Moustakas J., Diamond-Stanic A. M., 2007, *ApJ*, 663, L77  
Tucker W., David L. P., 1997, *ApJ*, 484, 602  
Vernaleo J. C., Reynolds C. S., 2006, *ApJ*, 645, 83  
Wang J.-M., Chen Y.-M., Hu C., 2006, *ApJ*, 637, L85  
Weymann R. J., Scott J. S., Schiano A. V. R., Christiansen W. A., 1982, *ApJ*, 262, 497  
Woods D. T., Klein R. I., Castor J. I., McKee C. F., Bell J. B., 1996, *ApJ*, 461, 767  
Yuan, F., Xie, F., & Ostriker, J. P. 2009, *ApJ*, 691, 98  
Zanni C., Murante G., Bodo G., Massaglia S., Rossi P., Ferrari A., 2005, *A&A*, 429, 399